# Supporting Information

## Rational Design of a Promising Oxychalcogenide Infrared Nonlinear Optical Crystal

Yansong Cheng,[a] Hongping Wu,[a] Hongwei Yu,*[a] Zhanggui Hu,[a] Jiyang Wang, [a] and Yicheng Wu[a]

[a] *Tianjin Key Laboratory of Functional Crystal Materials, Institute of Functional Crystal, Tianjin University of Technology, Tianjin 300384, China*
*To whom correspondence should be addressed: hwyu15@gmail.com*

**CONTENTS**

## Experimental Procedures

### Synthesis

**Reagents.** The starting materials including SrS (99.9%, Tianjin Hengshan Chemical, Reagent Co., Ltd.), ZnO (99.9%, Aladdin Chemical Reagent Co., Ltd.), Sn and S (99.99%, Beijing Hawk Science & Technology Co., Ltd.) were commercially purchased and stored in a glovebox filled with purified Ar (moisture and oxygen level is less than 0.1 ppm).

**Solid-State Synthesis.** $Sr_2ZnSn_2OS_6$ was synthesized via the conventional solid-state reaction method. First, 0.239 g of SrS, 0.081 g of ZnO, 0.237 g of Sn and 0.128 g of S were mixed according to the molar ratio of 2:1:2:4 and then ground and transferred into fused-silica tubes in a glovebox. The mixture was heated to 700 °C in 10 h and kept for 20 h and then cooled down to 25 °C in 10 h. The product was reground and heated again by the same procedure to improve the homogeneity and purity.

**Crystal Growth.** The millimeter-size crystal of $Sr_2ZnSn_2OS_6$ was grown by the solution method with SrS as the flux. A mixture of SrS (3 mmol, 0.359 g), ZnO (1 mmol,0.081 g), Sn (2 mmol, 0.237 g), and S (4 mmol, 0.128 g) was loaded into a graphite crucible, and this graphite crucible was put into a flame-sealed silica tube with a vacuum degree under $10^{-3}$ Pa. Then the tube was heated to 850 °C, held at this temperature for one day, and then cooled it down to 450 °C at the rate of 120 $^{o}$C/days. Finally, it was cooled to room temperature with the furnace was shut down. The products were carefully washed with N, N-dimethylformamide (DMF) to remove other byproducts and then dried in 50 °C. Many colorless and flaky crystals (70% yield based on Sn) with a small amount of unreacted SrS were discovered (Figure S2). Remarkably, $Sr_2ZnSn_2OS_6$ was placed in air for one month. No any hygroscopy or deterioration was observed. That indicates $Sr_2ZnSn_2OS_6$ has the excellent chemical stability.

### Powder X-ray Diffraction

Powder X-ray diffraction analyse was carried out at room temperature on a SmartLab 9KW X-ray diffractometer equipped with Cu *Kα* radiation (λ = 1.5418 Å). The data

was collected in the 2$\theta$ range of 10−70° with a step size of 0.01° and a step time of 2$s$. The powder XRD pattern shows good agreement with the calculated XRD pattern from the single-crystal model.

**Single-Crystal X-ray Diffraction**

A Bruker SMART APEX II diffractometer equipped with a 4K CCD detector using Mo Kα radiation (λ= 0.71073 Å) was used to collect the single-crystal XRD data at 296(2) K, and the data were integrated with a SAINT program. The crystal structure was solved by the direct method, and refined by the SHELXTL system. All of the atomic positions were refined by full matrix least-squares techniques. The structure was checked for missing symmetry elements with PLATON. The crystal data and structural refinement information are summarized in Table S1. The final refined atomic positions and isotropic thermal parameters and selected bond lengths and angles are listed in Tables S2 and S3.

**Infrared Spectroscopy**

The IR data was measured by a Nicolet iS50 FT-IR spectrometer in the range of 5−25 μm at room temperature. A $Sr_2ZnSn_2OS_6$ crystal was used for the IR measurement with a sample size of 0.4 mm × 0.8 mm.

**Raman Spectroscopy**

The Raman spectra of title compounds were collected on a Witec Raman Evolution spectrometer equipped with a CCD detector using 532 nm radiations from a diode laser. The sample was simply placed on a glass slide and a 50 objective lens was used to choose the area of the crystal specimens to be measured. A beam with the diameter of 35 μm and maximum power of 60 mW was used, and spectrum data collection was finished in 15 s.

**UV−Vis−NIR Diffuse Reflectance Spectroscopy**

The UV−Vis−NIR diffuse reflectance spectrum was measured with a Shimadzu SolidSpec-3700DUV UV−vis−NIR spectrophotometer at room temperature. The measurement range was from 240 to 2500 nm, and the barium sulfate is used as the diffuse reflection standard. Absorption (K/S) data was calculated from the following Kubelka–Munk function: $F(R) = (1-R)^2/2R = K/S$, R represents the reflectance, K

represents the absorption, and S represents the scattering factor.

**LDT Measurements**

LDTs were measured using a 1064 nm Q-switch laser with powdered $AgGaS_2$ sample as the reference. The detailed test procedure is as follows: the LDTs of $Sr_2ZnSn_2OS_6$ were evaluated on microcrystal powders (150−180 μm) with a pulsed YAG laser (1.06 μm, 10 ns, 10 Hz). Similar size of $AgGaS_2$ is chosen as the reference. With increasing laser energy, the color change of the powder sample is constantly observed by an optical microscope to determine the damage threshold. The damage spots and power of the laser beam were measured by a vernier caliper and an energy sensor, respectively.

**Powder SHG Test**

Powder SHG responses were measured according to the Kurtz−Perry method with Q-switched Nd:YAG lasers at the wave length of 2090 nm. Polycrystalline powder of $Sr_2ZnSn_2OS_6$ was classified into several different standard sizes: 53-75, 75-106, 106-120, 120-150 and 150-180 μm. Sieved $AgGaS_2$ powder was used as a reference. The intensity of the frequency-doubled output emitted from the sample was measured using a photomultiplier tube.

**Electronic structure calculations**

The electronic and band structure, as well as optical property calculation, were performed by employing CASTEP, with the norm-conserving pseudopotentials (NCPs). The Perdew−Burke−Ernzerhof (PBE) functional within the generalized gradient approximation (GGA) was applied for the exchange-correlation potential. The valence electrons of title compounds were calculated as Sr $4p^6 5s^2$ Zn $3p^6 3d^{10} 4s^2$, Sn $5s^2 5p^2$, S $3s^2 3p^4$, O $2s^2 2p^4$. The energy cutoff of plane wave's basis sets of them are 830 eV. Monkhorst-Pack k-point[10] was sampled with a separation of 0.03 $Å^{-1}$. We kept the default values of the CASTEP code on the aspect of the other calculation parameters and convergent criteria.

For the optical property calculation, the scissors-corrected GGA method is adopted, where the scissors operator is set as the difference between the calculated experimental/HSE06 and GGA bandgaps. This self-consistent ab initio approach has

been proven to be a very efficient and accurate way for the investigation of linear and nonlinear optical properties in many types of NLO materials without introducing any experimental parameter.

The so-called length-gauge formalism derived by Aversa and Sipe was adopted. At a zero frequency, the static second-order nonlinear susceptibilities can be ascribed to Virtual-Hole (VH) and Virtual-Electron (VE) processes,

$$X_{\alpha\beta\gamma}^{(2)} = X_{\alpha\beta\gamma}^{(2)}(VE) + X_{\alpha\beta\gamma}^{(2)}(VH)$$

Where , $X_{\alpha\beta\gamma}^{(2)}(VE)$ and $X_{\alpha\beta\gamma}^{(2)}(VH)$ are computed with the formulas as follows:

$$X_{\alpha\beta\gamma}^{(2)}(VE) = \frac{e^3}{2\hbar^2 m^3}\sum_{vcc'}\int\frac{d^3k}{4\pi^3}P(\alpha\beta\gamma)\mathrm{Im}\,[P_{cv}{}^{\alpha}P^{\beta}{}_{cc'}P_{c'v}{}^{\gamma}]\left(\frac{1}{\omega_{cv}{}^3\omega^2{}_{vc'}}+\frac{2}{\omega_{vc}{}^4\omega_{c'v}{}^2}\right)$$

$$X_{\alpha\beta\gamma}^{(2)}(VH) = \frac{e^3}{2\hbar^2 m^3}\sum_{vv'c}\int\frac{d^3k}{4\pi^3}P(\alpha\beta\gamma)\mathrm{Im}\,[P^{\alpha}{}_{vv'}P^{\beta}{}_{cv'}P_{cv}{}^{\gamma}]\left(\frac{1}{\omega_{cv}{}^3\omega^2{}_{v'c}}+\frac{2}{\omega_{vc}{}^4\omega_{cv'}{}^2}\right)$$

Here, α, β, γ are Cartesian components, and v/v', c/c' denote valence bands (VBs) and conduction bands (CBs). And $P(\alpha\beta\gamma)$, $\hbar\omega ij$ and $P_{ij}^{\alpha}$ refer to full permutation, the band energy difference and momentum matrix elements, respectively. Owing to the discontinuity of exchange correlation energy, the experimental value is usually larger than that of calculated band gap. Thus, scissor operator was used to make the conduction bands agree with the experimental values.

**The Birefringence Experiment**

The birefringence of $Sr_2ZnSn_2OS_6$ was measured by a Nikon Eclipse polarizing microscope E200MV POL equipped with a visible light filter. According to crystal optics, the retardation is proportional to birefringence and thickness of crystal. The specific formula is R = Δn × d, where R, Δn and d represent retardation, birefringence and thickness of crystal, respectively.

**Table S1.** Crystal data and structure refinement for $Sr_2ZnSn_2OS_6$.

| **Empirical formula** | **$Sr_2ZnSn_2OS_6$** |
|---|---|
| Formula weight | 686.35 |
| Temperature(K) | 293(2) |
| Wavelength(Å) | 0.71073 |
| Crystal system | Tetragonal |
| Space group | $P\bar{4}2_1m$ |
| Unit cell dimensions(Å) | $a$ = 9.664<br>$c$ = 6.330 |
| Volume(Å$^3$) | 591.1 |
| Z, Calculated density(g/cm$^3$) | 2, 3.856 |
| Absorption coefficient(mm$^{-1}$) | 16.140 |
| F(000) | 620 |
| Crystal size | 0.047 mm × 0.062 mm × 0.085 mm |
| Theta range for data collection | 2.981 to 27.467 |
| Reflections collected / unique | 6026/738<br>[$R_{(int)}$ = 0.0493] |
| Completeness to theta = 25.242 | 100.00% |
| Goodness-of-fit on F$^2$ | 1.044 |
| Final R indices [I>2sigma(I)] | $R_1$ = 0.0207<br>$wR_2$ = 0.0346 |
| R indices (all data) | $R_1$ = 0.0243<br>$wR_2$ = 0.0357 |
| Absolute structure parameter | 0.04 |
| Largest diff. peak and hole (e.Å$^{-3}$) | 0.859 and -0.473 |

**Table S2.** (a) Selected bond lengths (Å) and angles (deg.) for $Sr_2ZnSn_2S_6O$.

| | | | |
|---|---|---|---|
| Sn(1)-O(6) | 2.029(4) | O(6)-Sr(2)-S(4)#6 | 75.27(11) |
| Sn(1)-S(4) | 2.321(2) | S(4)#4-Sr(2)-S(4)#6 | 143.25(3) |
| Sn(1)-S(5)#1 | 2.3658(16) | S(4)#5-Sr(2)-S(4)#6 | 71.73(7) |
| Sn(1)-S(5) | 2.3658(16) | O(6)-Sr(2)-S(5)#7 | 67.74(6) |
| Sr(2)-O(6) | 2.788(5) | S(4)#4-Sr(2)-S(5)#7 | 83.78(4) |
| Sr(2)-S(4)#4 | 3.113(2) | S(4)#5-Sr(2)-S(5)#7 | 130.94(5) |
| Sr(2)-S(4)#5 | 3.1253(17) | S(4)#6-Sr(2)-S(5)#7 | 68.60(5) |
| Sr(2)-S(4)#6 | 3.1253(17) | O(6)-Sr(2)-S(5) | 67.74(6) |
| Sr(2)-S(5)#7 | 3.1357(17) | S(4)#4-Sr(2)-S(5) | 83.78(4) |
| Sr(2)-S(5) | 3.1357(17) | S(4)#5-Sr(2)-S(5) | 68.60(5) |
| Sr(2)-S(5)#8 | 3.1498(17) | S(4)#6-Sr(2)-S(5) | 130.94(5) |
| Sr(2)-S(5)#9 | 3.1498(17) | S(5)#7-Sr(2)-S(5) | 121.07(7) |
| Zn(3)-S(5)#4 | 2.3328(16) | O(6)-Sr(2)-S(5)#8 | 143.81(3) |
| Zn(3)-S(5)#10 | 2.3328(16) | S(4)#4-Sr(2)-S(5)#8 | 68.58(4) |
| Zn(3)-S(5)#11 | 2.3328(16) | S(4)#5-Sr(2)-S(5)#8 | 81.90(4) |
| Zn(3)-S(5) | 2.3328(16) | S(4)#6-Sr(2)-S(5)#8 | 123.44(5) |
| O(6)-Sn(1)-S(4) | 116.0(2) | S(5)#7-Sr(2)-S(5)#8 | 145.07(3) |
| O(6)-Sn(1)-S(5)#1 | 97.58(14) | S(5)-Sr(2)-S(5)#8 | 77.98(6) |
| S(4)-Sn(1)-S(5)#1 | 119.00(5) | O(6)-Sr(2)-S(5)#9 | 143.81(3) |
| O(6)-Sn(1)-S(5) | 97.58(13) | S(4)#4-Sr(2)-S(5)#9 | 68.58(4) |
| S(4)-Sn(1)-S(5) | 119.00(5) | S(4)#5-Sr(2)-S(5)#9 | 123.44(5) |
| S(5)#1-Sn(1)-S(5) | 103.65(8) | S(4)#6-Sr(2)-S(5)#9 | 81.90(4) |
| O(6)-Sr(2)-S(4)#4 | 116.92(14) | S(5)#7-Sr(2)-S(5)#9 | 77.98(6) |
| O(6)-Sr(2)-S(4)#5 | 75.27(11) | S(5)-Sr(2)-S(5)#9 | 145.07(3) |
| S(4)#4-Sr(2)-S(4)#5 | 143.25(3) | S(5)#8-Sr(2)-S(5)#9 | 72.38(6) |

Symmetry transformations used to generate equivalent atoms:

#1 y-1/2,x+1/2,z #2 -x+1,-y+2,z #3 -y+1,x,-z

#4 y,-x+1,-z+1 #5 x,y,z-1 #6 -x+1,-y+2,z-1

#7 -y+3/2,-x+3/2,z #8 y,-x+1,-z #9 x+1/2,-y+3/2,-z

#10 -x+1,-y+1,z #11 -y+1,x,-z+1 #12 x,y,z+1

#13 -x+1,-y+2,z+1

**Table S3.** Atomic coordinates (× $10^4$) and equivalent isotropic displacement parameters ($A^2 \times 10^3$) for $Sr_2ZnSn_2S_6O$ $U_{(eq)}$ is defined as one third of the trace of the orthogonalized $U_{ij}$ tensor.

| Atoms | x | y | z | U(eq) | BVS |
|---|---|---|---|---|---|
| Sn(1) | 3674(2) | 8674(2) | 647(3) | 17(1) | 4.04 |
| Zn(1) | 0 | 10000 | 0 | 17(1) | 2.00 |
| S(1) | 3658(7) | 8658(7) | 2897(11) | 20(2) | 2.14 |
| S(2) | 1667(7) | 9367(7) | 2368(9) | 19(2) | 2.08 |
| O(1) | 5000 | 10000 | 1930(40) | 17(9) | 1.73 |
| Sr(1) | 6590(1) | 8410(1) | 4933(3) | 20(1) | 2.12 |

**Table S4. The powder LDTs of $AgGaS_2$ and $Sr_2ZnSn_2OS_6$**

| Compound | Damage energy (mJ) | Spot diameter (mm) | τp (ns) | Laser damage threshold [MW $cm^{-2}$] |
|---|---|---|---|---|
| $Sr_2ZnSn_2OS_6$ | 19.8 | 2.4 | 10 | 131 |
| $AgGaS_2$ | 6.9 | 2.4 | 10 | 12 |

**Table S5.** Dipole Moment Direction and Magnitude (in Debye) of $[ZnS_4]$ and $[SnOS_3]$ in $Sr_2ZnSn_2S_6O$

| | Species | a | b | c | Magnitude |
|---|---|---|---|---|---|
| **$Sr_2ZnSn_2OS_6$** | $[ZnS_4]^{6-}$ | 0 | 0 | 0 | 0 |
| | $[SnOS_3]^{4-}$ | 4.017 | -4.017 | 3.676 | 6.767 |

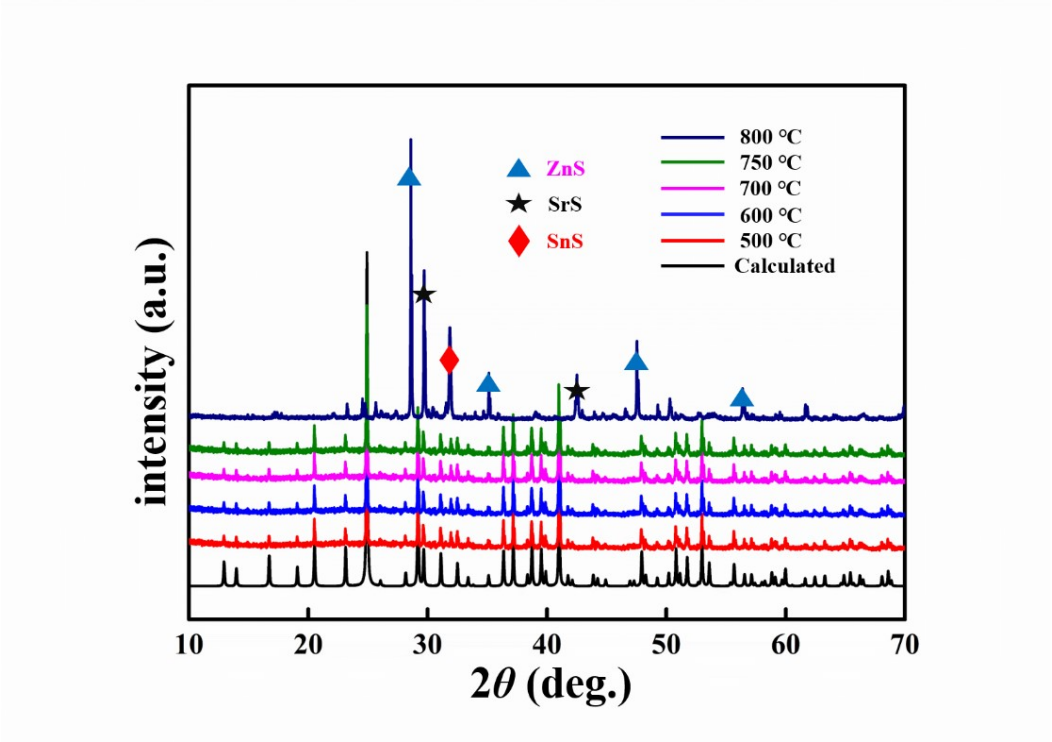


**Figure S1.** powder XRD patterns of $Sr_2ZnSn_2OS_6$ at different temperatures.

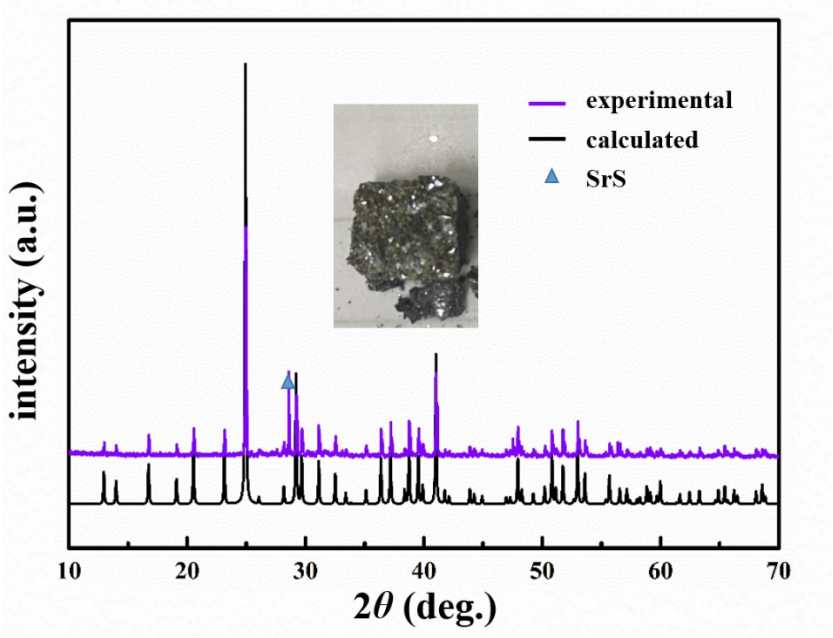


**Figure S2.** The powder XRD patterns of $Sr_2ZnSn_2OS_6$ yield. The inserted photograph is the yield.

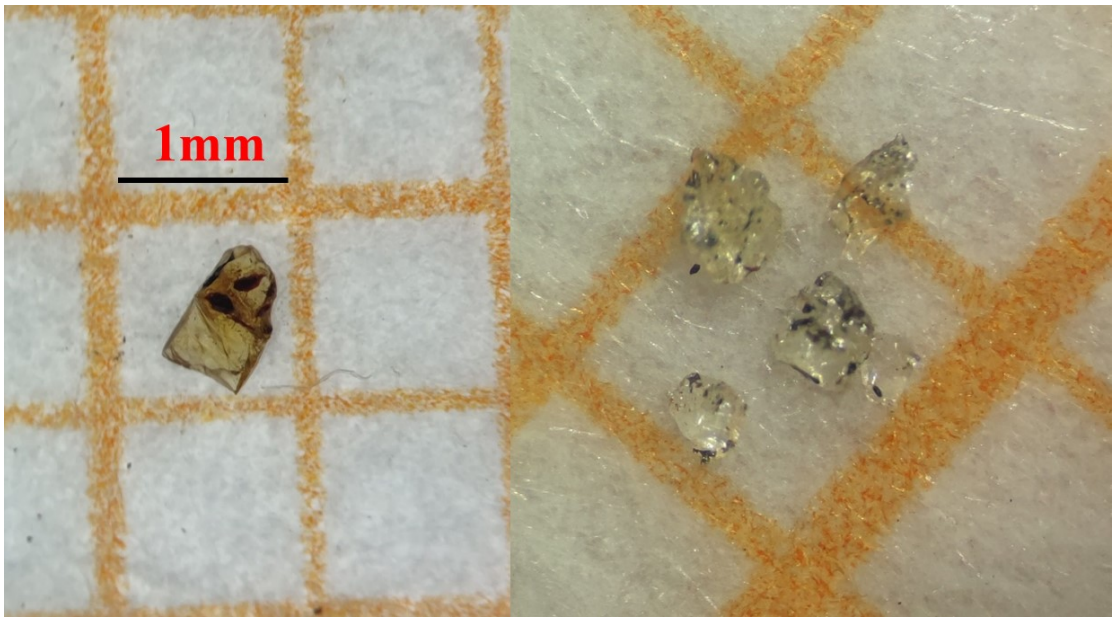


**Figure S3.** photograph of $Sr_2ZnSn_2OS_6$ crystals.

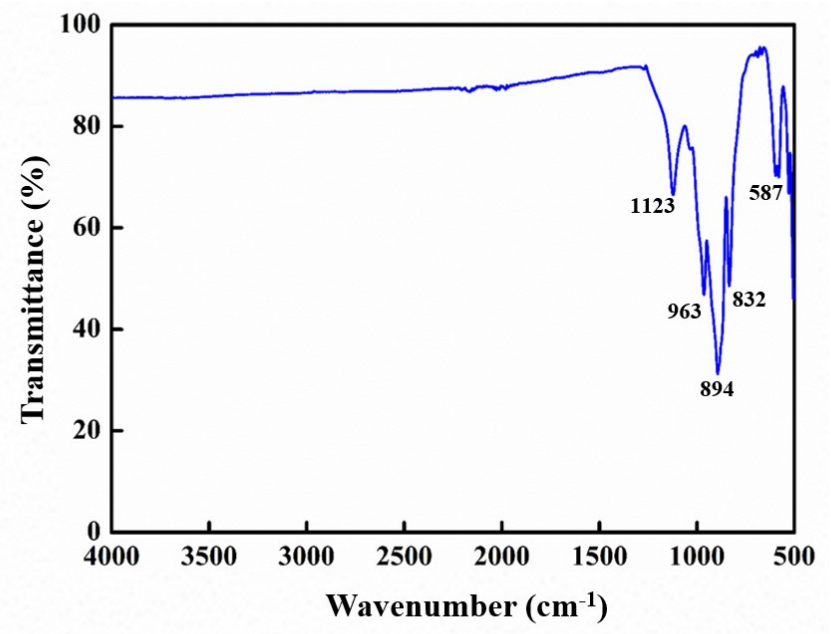


**Figure S4.** IR spectrum of $Si_2ZnSi_2O_7$.

**Figure S5.** The crystal quality of $AgGaS_2$.

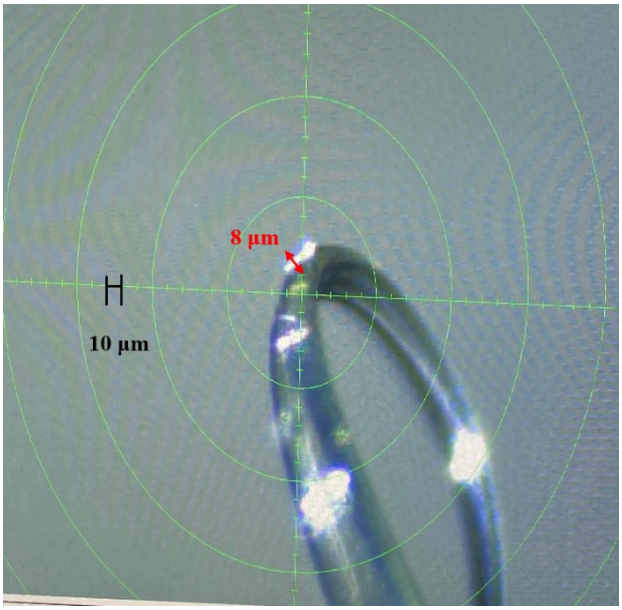


**Figure S6.** Crystal size photo of $Sr_2ZnSn_2S_6O$

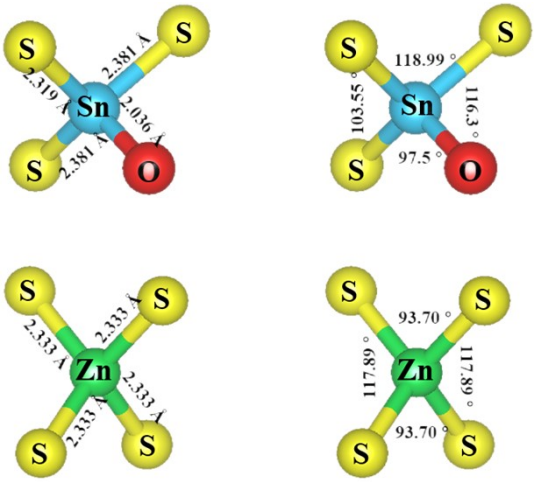


**Figure S7.** The bond lengths and angles of $SnOS_3$ and $ZnS_4$.

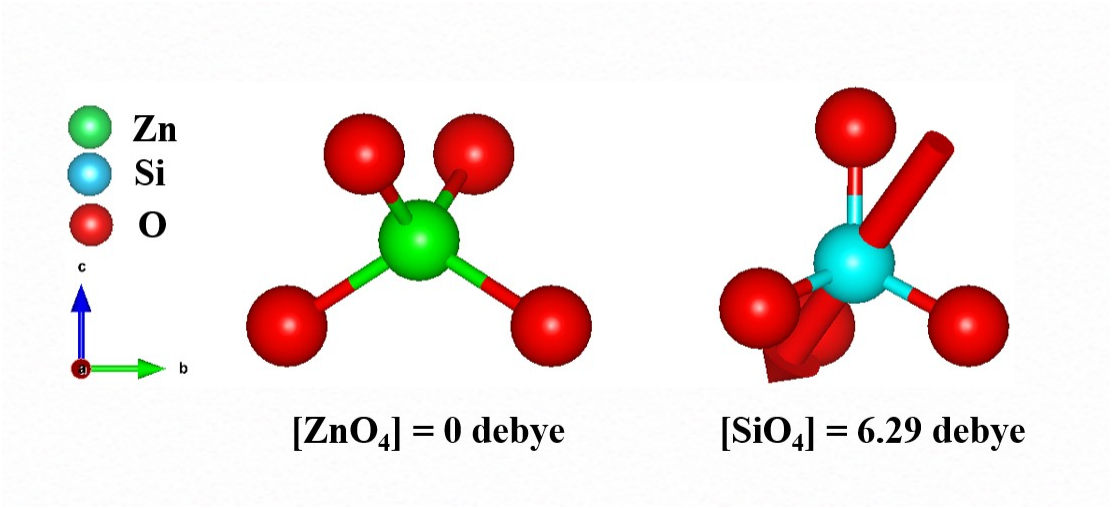


**Figure S8.** Dipole moment magnitudes (in Debye) and directions for the $[ZnO_4]$ and $[SiO_4]$ tetrahedra in $Sr_2ZnSi_2O_7$